

## Topological and conventional nanophotonic waveguides for directional integrated quantum optics

N. J. Martin <sup>1,\*</sup>, M. Jalali Mehrabad,<sup>2</sup> X. Chen,<sup>1</sup> R. Dost,<sup>1</sup> E. Nussbaum <sup>3</sup>, D. Hallett,<sup>1</sup> L. Hallacy,<sup>1</sup> A. Foster,<sup>1</sup> E. Clarke <sup>4</sup>,  
P. K. Patil <sup>4</sup>, S. Hughes,<sup>3</sup> M. Hafezi,<sup>2</sup> A. M. Fox,<sup>1</sup> M. S. Skolnick,<sup>1</sup> and L. R. Wilson<sup>1</sup>

<sup>1</sup>Department of Physics and Astronomy, University of Sheffield, Sheffield S3 7RH, United Kingdom

<sup>2</sup>Joint Quantum Institute, University of Maryland, College Park, Maryland 20742, USA

<sup>3</sup>Centre for Nanophotonics, Department of Physics, Engineering Physics and Astronomy, Queen's University, Kingston, Ontario, K7L 3N6, Canada

<sup>4</sup>EPSRC National Epitaxy Facility, University of Sheffield, Sheffield S1 4DE, United Kingdom



(Received 20 January 2024; revised 2 April 2024; accepted 29 April 2024; published 20 June 2024)

Directionality in integrated quantum photonics has emerged as a promising route towards achieving scalable quantum technologies with nonlinearities at the single-photon level. Topological photonic waveguides have been proposed as a novel approach to harnessing such directional light-matter interactions on-chip. However, uncertainties remain regarding the strength of the directional coupling of embedded quantum emitters to topological waveguides in comparison to conventional line defect waveguides. In this work we present an investigation of directional coupling in a range of waveguides using a combination of experimental, theoretical, and numerical analyses. We quantitatively characterize the position dependence of the light-matter coupling on several topological photonic waveguides and benchmark their directional coupling performance against conventional line defect waveguides. We conclude that topological waveguides underperform in comparison to conventional line defect waveguides, casting their directional optics credentials into doubt. To demonstrate this is not a question of the maturity of the field; we show that state-of-the-art inverse design methods, while capable of improving the directional emission of these topological waveguides, still place them significantly behind the operation of a conventional (glide-plane) photonic crystal waveguide. Our results and conclusions pave the way towards improving the implementation of quantitatively predicted quantum nonlinear effects on-chip.

DOI: [10.1103/PhysRevResearch.6.L022065](https://doi.org/10.1103/PhysRevResearch.6.L022065)

**Introduction.** Integrated nanophotonic platforms in which embedded quantum emitters are interfaced with optical waveguides and cavities on-chip are a promising route towards scalable quantum technologies. An attractive property of nanophotonic waveguides is their support for directional light-matter interactions, whereby an emitter with a circularly polarized transition dipole moment couples unidirectionally at the single-photon level to a single-photon-waveguide mode [1–4]. While this spin-orbit coupling is often described as “chiral” (as the direction of the emission depends on the handedness of the transition dipole moment), the symmetry of the waveguide geometry and the structure of the quantum dot is preserved. Such interactions have previously been demonstrated on-chip using semiconductor quantum dots (QDs) coupled to photonic crystal (PhC) line defects such as W1 [3] and glide-plane [2,5,6] waveguides.

Recently, PhC topological waveguides have received significant interest for integrated nanophotonics due to their attractive properties, which include robust transmission around

tight bends [7–15], opening up their applications to more complex guided structures such as ring resonators, beam splitters, and filters that require sharp bends [16–19].

More pertinently for directional quantum optics, topological waveguides were envisioned to have two key properties: (1) robustness to in-plane backscattering, and (2) intrinsic unidirectional emission for embedded emitters, with the unidirectional emission expected to arise from the intrinsically helical edge modes which arise at the interface between two topologically distinct PhCs [7,15,20].

Despite intense research on the application of these systems, experimental measurement of the degree of robustness to backscattering of these waveguides was only very recently examined using external light sources [21], the results casting considerable doubt on the resistance to backscattering. However, an experimental investigation into the envisioned property of intrinsic unidirectional emission of topological waveguides, key to their directional quantum optics applications, remains missing.

As in conventional, nontopological waveguides, directional coupling of an embedded emitter to a topological photonic waveguide is position dependent. In the most extreme case, the direction of emission from a circularly polarized transition can be completely reversed by moving it within a unit cell of the PhC lattice. While the properties of conventional waveguides and topological waveguides have been compared in simulations [22], here we use both simulations and

\*n.j.martin@sheffield.ac.uk

experiment to compare these approaches to realizing directional light-matter interactions on-chip.

Within the main text we present data on conventional W1, glide-plane, zigzag interface, valley-Hall (VH), and bearded-interface VH waveguides, focusing on topological PhC interface types in which QD integration has previously been demonstrated [9,13,18]. In addition, we include a version of the bearded-interface VH waveguide that is optimized using inverse design techniques. (See Supplemental Material [23] for a discussion of slab waveguides and an optimized glide-plane waveguide [6].) For each waveguide we present the dispersion relation of the guided mode, the spatial electric field intensity, and degree of circular polarization, as well as the spatial and wavelength dependence of the  $\beta$  factor (see Sec. III A) for emitters within the waveguides. We use this simulated data to make predictions for the expected distribution of the directional contrast of embedded QDs and then determine experimentally the directional contrast for a large number of QDs in each type of structure, showing good agreement with the simulations. While the topological waveguides, optimized through inverse design, demonstrate promising improvements in directional properties in simulation, our experimental results also serve to highlight the limitations of current approaches. In particular, we stress the need to develop waveguides which support high- $\beta$  factors while simultaneously showing near-unity directional coupling.

*Photonic-crystal-waveguide designs for directional quantum optics.* The PhC waveguides considered in this work are described schematically in Figs. 1(a)–1(e). We consider two conventional (i.e., nontopological) and three nontrivial topological designs. For each type of waveguide we show

- (i) The waveguide design.
- (ii) The band structure.
- (iii) The electric field profile.
- (iv) The directionality ( $S_3$ ).
- (v) The  $\beta$  factor.
- (vi)  $S_3$  and E-field probability density plots.

For each type of waveguide we focus on the parts of the band structure shaded in blue, and the field profiles in panels (iii)–(v) are calculated for the points shown by the red circle in panel (ii). The first conventional design [shown in Fig. 1(a)] is that of a W1 waveguide, comprising a triangular lattice of circular holes etched into a thin dielectric membrane, with one row of holes omitted in the  $\Gamma$ -K direction to form a line defect. As shown in Fig. 1(a) (ii), several guided Bloch modes can be observed within the PhC band gap of the W1 waveguide; we focus on the lowest frequency mode, with the field profile shown in Fig. 1(a) (iii), which has an electric field antinode at the center of the waveguide.

The second conventional design studied here is the glide-plane waveguide, which is formed by displacing the holes on one side of a W1 waveguide by half the lattice period along the waveguide. The transverse electric (TE)-like mode dispersion diagram for the glide-plane structure is shown in Fig. 1(b) (i). We focus on the single-mode region of the higher-frequency mode, as the multimode region where the two modes overlap spectrally prevents directional coupling being realized [5]. The field profile for this mode is shown in Fig. 1(b) (iii).

The conventional waveguides introduced above are compared in this work with three topologically nontrivial

structures. We have chosen valley-Hall waveguides, as their interfaces support guided optical modes lying below the light line, unlike the alternative spin-Hall approach [7,17,24]. VH waveguides can be formed by interfacing two VH photonic crystals where the unit cell is a rhombus containing a pair of apertures of differing sizes in two distinct ways. The first, the zigzag interface, is an interface of these two crystals with mirror symmetry. For this work a design for the zigzag interface is comprised of triangular apertures, with the larger triangles at the interface. This design is chosen for its favorable band structure, with the dispersion diagram in Fig. 1(c) (ii) showing that the waveguide supports a single guided TE mode, with the mode profile given in Fig. 1(c) (iii). The bearded interface, in contrast, is formed by interfacing two VH photonic crystals such that it forms a glide-plane symmetric interface. For this work the original bearded-interface waveguide is formed of circular apertures, with the smaller of the apertures at the interface. We have also included an optimized version of the bearded interface within our investigation. Here, an inverse design algorithm was used to optimize the geometrical parameters of a bearded-interface VH nanophotonic waveguide for high  $\beta$  factors and strong directional light-matter interactions (see Supplemental Material, Sec. S1, for more details on the inverse design process [23]).

*Simulation of the waveguide  $\beta$ -factor, E-field properties, and directionality.* This section presents simulation results that quantify the spatial dependence of the  $\beta$  factor, E field, and directional contrast. This includes a description of the model used to predict the directional statistics, i.e., the expected statistical distribution of directional contrast for a large number of randomly positioned QDs.

*a.  $\beta$  factor.* We define our  $\beta$  factor as the ratio of the spontaneous emission rate of an emitter into an intended guided mode compared to the total decay rate. To calculate the  $\beta$  factor we used finite-difference time-domain (FDTD) simulations to calculate the fraction of radiative power coupled into propagating modes over the total power injected from the emitter. To determine the spatial distribution of the  $\beta$  factor, we vary the dipole position within a region from approximately  $-2a$  to  $+2a$  ( $a$  being the lattice constant of the bulk photonic crystal) from the waveguide center, excluding regions within the apertures of the waveguides (see Supplemental Material, Secs. S3–S5 for more information on the calculation of the  $\beta$  factor as well as its spectral dependence).

The relationship between the intensity of the electric field at a given point to the  $\beta$  factor at that point can be seen by comparing the electric field profiles of Figs. 1(a)–1(e) (iii), and the  $\beta$  factors of Figs. 1(a)–1(e) (v), with areas of high electric field intensity resulting in higher  $\beta$  factors. However, the enhancement of the  $\beta$  factor arising from the slow light regions of the waveguides can result in regions with relatively low electric field intensities having high  $\beta$  factors, with this effect most notable within the W1. This wavelength dependence of the  $\beta$  factor is shown within the Supplemental Material (SM) and offers waveguides with poor E field and  $S_3$  overlap a route to high  $\beta$  factor at directional points.

*b. Stokes  $S_3$  parameter and directional contrast.* The directional properties of each waveguide were evaluated using guided-mode-expansion simulations [25] by calculating the

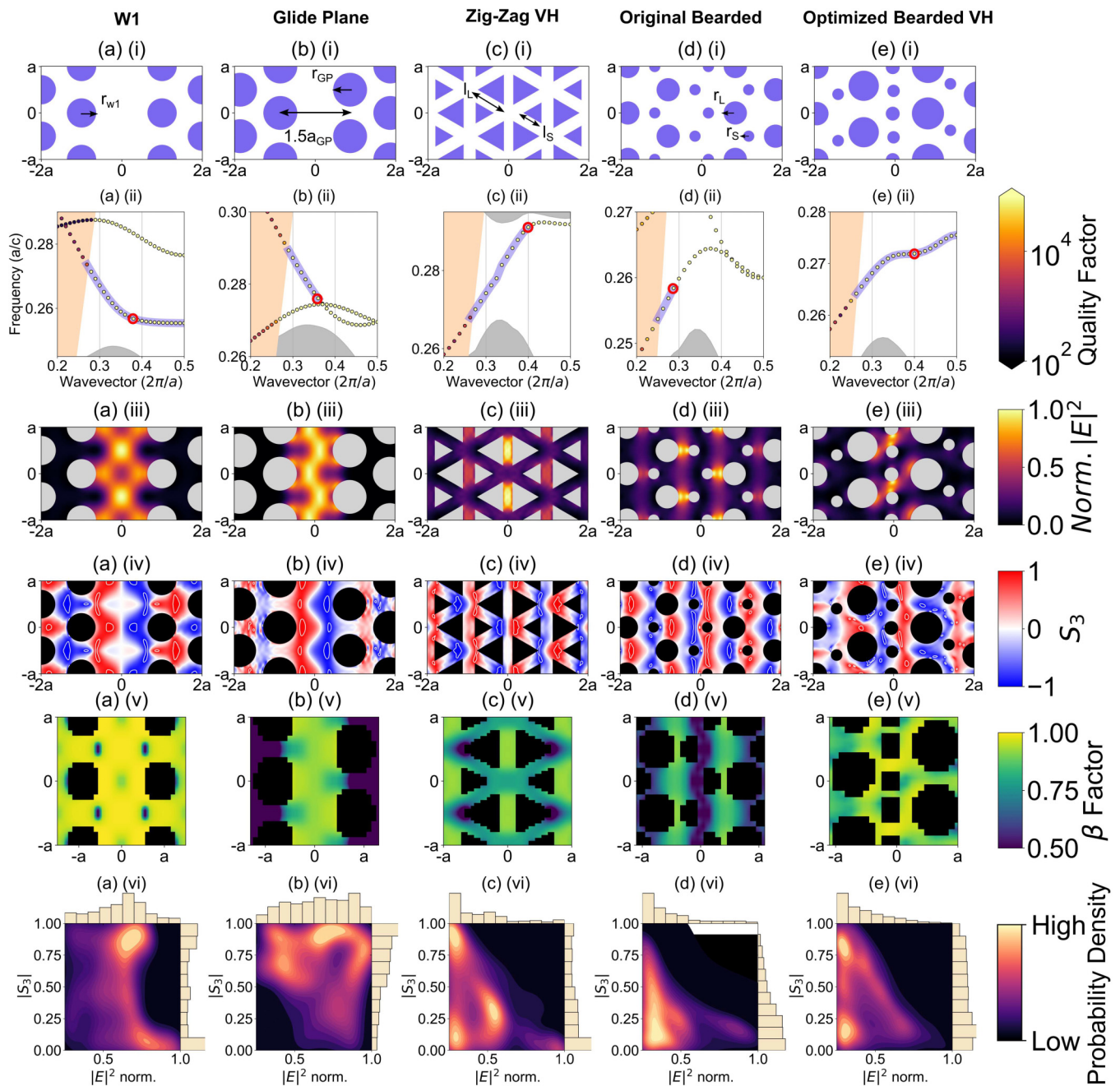


FIG. 1. (a–e) (i) Schematics of the (a) W1 waveguide, (b) glide-plane waveguide, (c) zigzag interface VH topological waveguide, (d) unoptimized bearded-interface VH topological waveguide, and (e) a bearded-interface VH topological waveguide optimized using an inverse design technique for a more favorable band structure and improved electric field and  $S_3$  overlap. (a)–(e) (ii) Simulated band structures of the waveguides, with the single-mode region of interest highlighted in blue, and the specific frequency of single-mode operation chosen for the electric field plots in the rest of the figure highlighted on the band structures in red. Radiative quality factors for the guided modes are indicated using the color bar on the right. The radiative quality factors for the guided modes are indicated by the color bar on the right. (a–e) (iii) Simulated electric field profiles and (a–e) (iv)  $S_3$  maps for the waveguides. Within (a–e) (iv), encircled white regions indicate regions where directional contrast is expected to be 95% and above. Band structures and electric field plots were simulated by guided-mode expansion. (a–e) (v) Spatial dependence within the waveguides of the  $\beta$  factor at the same frequency as the electric field plots, simulated using FDTD. Black regions indicate the position of the waveguide apertures. (a–e) (vi) Probability density plots showing the likelihood of a set of randomly positioned dots possessing a given  $S_3$  value for different electric field strengths within the waveguide interface. Areas of high-probability density indicate combinations of directional contrasts and electric field strengths that are more likely. The apertures of the waveguides are excluded from the calculations.

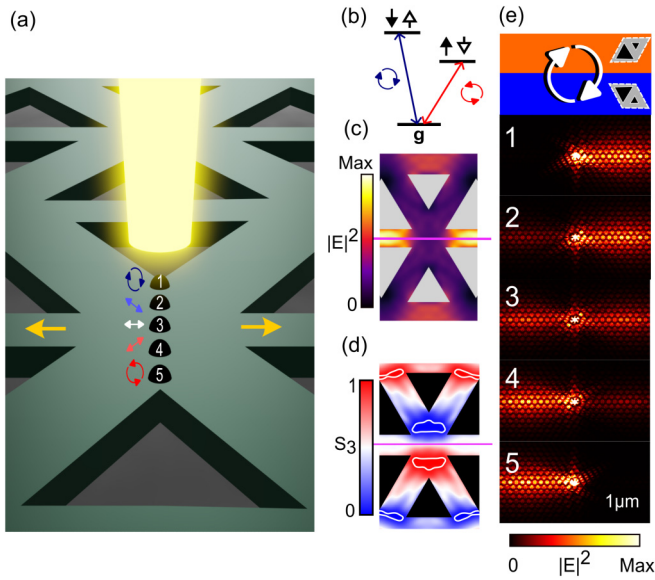


FIG. 2. (a) Schematic diagram showing the positional dependence of the direction of emission of a circularly-polarized dipole source within a VH waveguide; labels show the polarization of the local field at the different positions, with the waveguide interface highlighted in magenta. (b) Level diagrams and optical transitions for a neutral exciton QD state showing left- and right-circularly-polarized transitions. (c)  $|E|^2$  field profile within the VH waveguide interface. (d)  $S_3$ , degree of circular polarization at different points within the VH waveguide interface. Encircled white regions indicate regions where  $|S_3| \geq 0.95$ . (e) FDTD simulations showing the positional dependence of emission from a circularly polarized dipole at points 1–5 within the zigzag VH waveguide interface. The top of the figure shows the position of the waveguide interface between two topologically distinct photonic crystals (shown in orange and blue), as well as the central position of the right-circularly-polarized dipole source used in the simulations.

Stokes  $S_3$  parameter defined as

$$S_3 = \frac{-2\text{Im}(E_x E_y^*)}{|E_x|^2 + |E_y|^2}. \quad (1)$$

The simulated Stokes  $S_3$  parameter is shown in Figs. 1(a)–1(e) (iv) for the five waveguides. The Stokes parameter at the position of a QD determines the directional contrast of the emission. Figure 2 shows the relationship between the  $S_3$  parameter and the direction of emission of a circularly polarized emitter, such as the Zeeman split lines of a neutral exciton within a QD [Fig. 2(b)]. The directional contrast is defined as

$$C = \frac{T^R - T^L}{T^R + T^L}, \quad (2)$$

where  $T^R$  and  $T^L$  are the transmission right and left through a waveguide, respectively, for an emitter embedded within a linear waveguide. Within the FDTD simulations of Fig. 2, the directional coupling of a circularly polarized emitter (within the example of the VH zigzag interface) is shown to be position dependent due to the different  $S_3$  values at different points within the waveguide. While all five waveguides show regions of high directional contrast, with contrasts above 95%

indicated by the in-circled white regions of Figs. 1(a)–1(e) (iv),  $S_3$  does not give the complete picture of a waveguide’s suitability to directional quantum optics, as discussed in the next section.

*c. Coincidence of high-directionality and E-field concentration.* The likelihood of a set of randomly positioned QDs possessing a given  $S_3$  value for different electric field strengths within the waveguide interface is shown by the probability density plots of Figs. 1(a)–1(e) (iv). Areas of high probability density indicate combinations of directional contrasts and electric field strengths that are more likely; the air regions of the waveguides where there are no QDs are excluded from the calculations. Within these plots we see that the glide-plane waveguide has the best overlap of  $S_3$  and  $|E|^2$ . The W1 waveguide shows a high concentration of QDs at high  $S_3$  for  $|E|^2 = 0.7$ , which outperforms the distributions seen for the topological waveguides, characterized by low density at the intersection of high  $S_3$  and  $|E|^2$  found in the dark regions at the top right of the plots. The optimized bearded interface does, however, perform better than the un-optimized version in this regard, with the optimized waveguide showing a greater concentration of high-directionality QDs at  $|E|^2 = 0.3$ .

*d. Simulated directional statistics.* The directional statistics of the waveguides can be modelled by considering the  $S_3$  field maps for the waveguides over the selected waveguide regions highlighted in blue in Figs. 1(a)–1(e) (ii). The electric field data was calculated using guided-mode expansion for the middle of the slab (where the QDs are located) for multiple points within a  $10a$  ( $\pm 5a$  from the waveguide center) supercell of the waveguide. Then, to calculate the predicted directional statistics, we applied a minimum  $\beta$  factor and Purcell factor condition to remove waveguide regions that would not contribute to measurable quantum dot emission, with FDTD simulations providing data for the  $\beta$  factor [see Figs. 1(a)–1(e) (v)] and Purcell factor. This threshold was set so that only points within the waveguide that had a combined value for Purcell factor multiplied by a  $\beta$  factor above 0.5 were included ( $F_p \times \beta \geq 0.5$ ) and additionally, to account for the “dead zones” for QD emission that exist around the apertures of the waveguides. The extent of this dead zone can depend on the wafer properties and the presence of fabrication processes such as surface passivation [26]. For this reason we have calculated the expected statistics for the waveguides, excluding a region of both 15 and 30 nm [27] around the apertures. The absence of QD emission in proximity to the etched surfaces is likely to arise from detrimental effects of surface defects and interface roughness. The simulations of the directional statistics for the five types of waveguides are shown in Figs. 4(a)–4(e). These results will be discussed in the next section when they are compared to the experimental data.

*Method.*

*a. Experimental comparison of the photonic crystal waveguides.* The experimental results were obtained for devices fabricated in a 175-nm-thin GaAs *p-i-n* membrane containing a single layer of InAs QDs. Representative scanning electron microscopy (SEM) images of the waveguide interfaces are shown in Figs. 3(a)–3(e). Each waveguide was terminated on both ends with a grating coupler for light extraction into external optics, as shown in Fig. 3(j). The sample was cooled

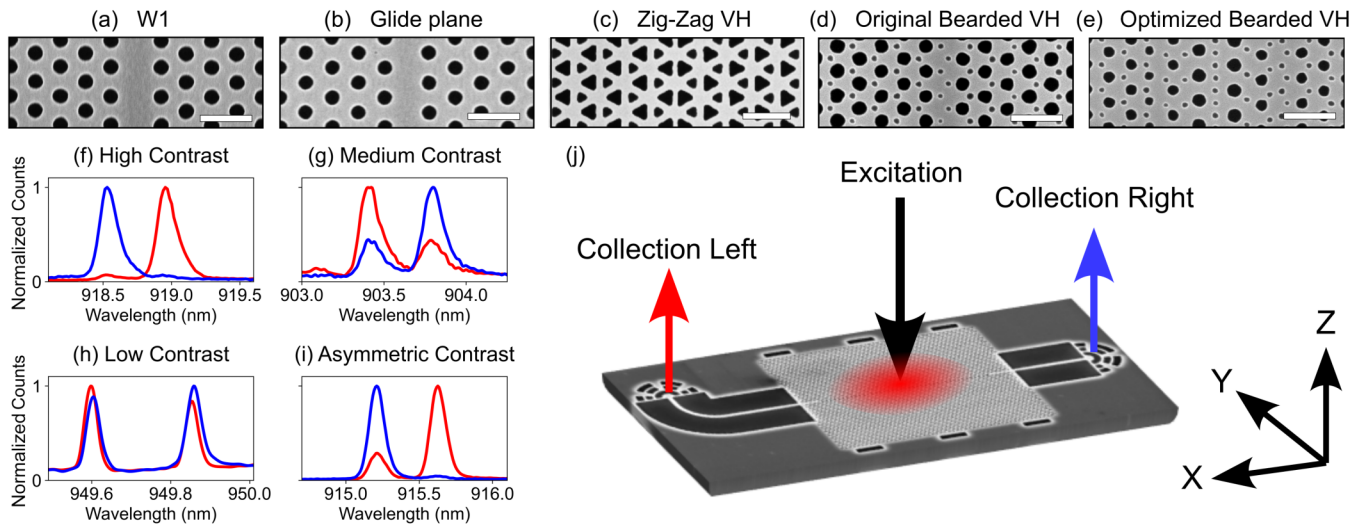


FIG. 3. SEM images of the fabricated waveguide for (a) W1, (b) glide plane, (c) zigzag VH, (d) original bearded VH, and (e) optimized bearded VH. Scale bars are  $0.4 \mu\text{m}$ . Examples of dot lines split by  $B \neq 0$  magnetic fields, with (f) high directional contrast, (g) medium contrast, (h) low contrast, and (i) asymmetric contrast. (j) Schematic of the on-chip device layout, indicating the location of the left out-coupler collection (red) and the right out-coupler collection (blue).

to 4.2 K in a superconducting magnet cryostat. To determine the operation bandwidth of each waveguide, broadband photoluminescence (PL) was generated by exciting the ensemble of QDs located within one grating coupler using nonresonant excitation ( $\lambda_{\text{laser}} = 810 \text{ nm}$ ). PL emission was then detected from the other out-coupler, with representative transmission spectra shown in SM Fig. S2. A combination of the identification of a sharp decrease in transmission resulting from the band edge of a guided mode and an analysis of the Fabry-Pérot fringes of the waveguide were used to identify the single-mode regions of interest. (More information on the identification of the single-mode regions of the waveguides can be found in SM Sec. S2.)

While in this study achievable  $\beta$  factors are estimated through simulations, the degree of directional emission was measured experimentally. We measured the directional contrast independently for a large number of individual QDs in each waveguide. To do so, we used low-power microphotoluminescence ( $\mu\text{PL}$ ) measurements, exciting nonresonantly from above the waveguide and collecting emission independently from the two out-couplers. The QD density was of the order of  $10^9 \text{ cm}^{-2}$ , which allowed for single emitters to be independently resolved. We focused on QDs spectrally located in the single-mode regions of the waveguides, highlighted in blue in Figs. 1(a)–1(e). In the presence of a Faraday-geometry magnetic field, the circularly polarized dipole transitions of

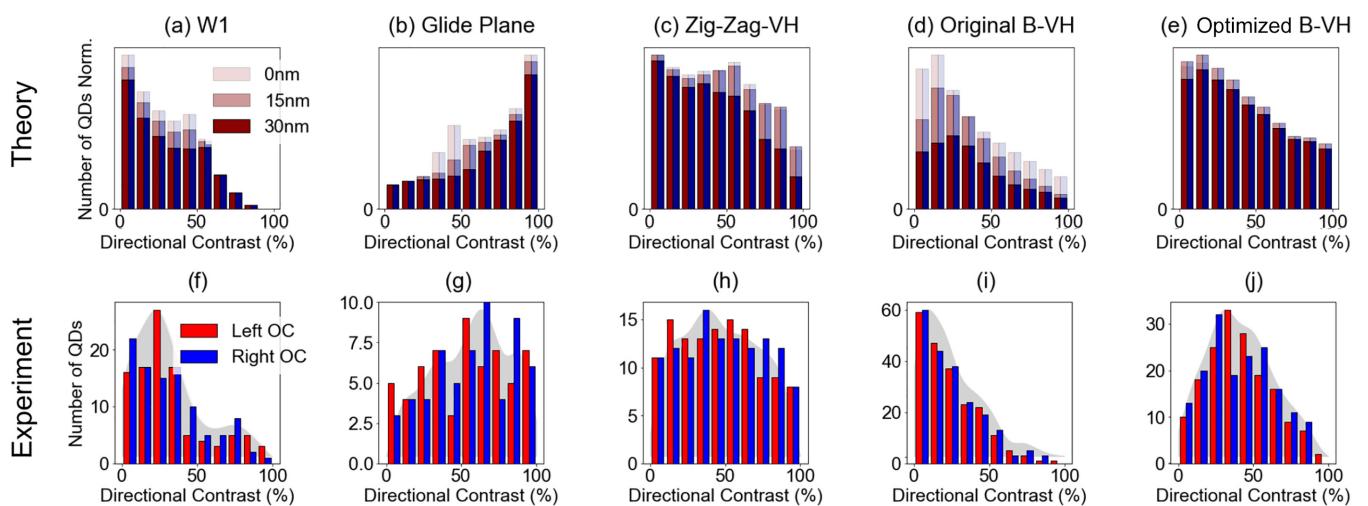


FIG. 4. (a)–(e) Modeled predictions for the directional statistics of the waveguides for a 0-nm and 15-nm and 30-nm dead zone, with the plots normalized to the 0-nm case to show the reduction in the expected number of dots that arise from these dead zones. (f)–(j) Directional contrast measured experimentally for randomly positioned QDs within the different waveguides. Left out-coupler data is presented in red and right out-coupler data in blue. All experimental data were recorded when an external magnetic field of  $B_z = 3 \text{ T}$  was applied. The gray background plot shows a smooth distribution of the directionality data, where no distinctions between the results of the left and right out-couplers are made.

the QD split energetically, allowing for them to be resolved independently within the spectral resolution of our detection.

We quantify the degree of directional coupling in each nanophotonic waveguide experimentally using randomly distributed self-assembled InAs QDs, distributed by growth in the  $xy$  plane at  $z = 0$  of the GaAs membrane [see Fig. 3(j) for axes]. The guided PL of single QDs is detected from right and left out-couplers [denoted as Left OC and Right OC in Figs. 4(f)–4(j)] at opposite ends of each waveguide.

To allow for the possibility of dissimilar out-coupler collection efficiency, the directional contrast was evaluated independently for each out-coupler using the relationship

$$C_i = \frac{I_i^{\sigma^+} - I_i^{\sigma^-}}{I_i^{\sigma^+} + I_i^{\sigma^-}}, \quad (3)$$

where  $I_i^{\sigma^j}$  ( $j = +, -, i = \text{left, right}$ ) represents the intensity of  $\sigma^j$ -polarized light emitted by the QD and collected from the left and right out-couplers.

Self-assembled growth leads to random positions of QDs within the  $xy$  plane, which leads to coupling of QDs placed at areas of the waveguide with a range of directional contrast. The results are shown in histogram graphs for the experimentally measured directional contrasts for each case. The binned histograms from the  $S_3$  parameters calculated via FDTD simulations, as discussed in Sec. 3.4, are also shown for comparison.

For the W1 waveguide we see that, in general, there is predicted to be a low proportion of QDs with a directionality  $> 80\%$  but a high proportion of dots with low directional contrast. This can be explained by both the concentration of the electric field being at points of low circular polarization, as seen in Figs. 1(f) and 1(k), and the annihilation of directional points at the band edge in a W1 waveguide [28]. The experimental results broadly agree with this prediction.

The glide-plane PhC waveguide exhibits the best directional coupling for QDs in both simulation and experiment. Nevertheless, there is a lower proportion of high-contrast QDs in experiment than expected. This may be explained by the glide plane's high-directional-contrast regions being located near the waveguides' etched areas.

The topological VH zigzag interface achieves a high proportion of QDs with high contrast but not as high as the glide plane, and as can be seen in Fig. 1(e) (vi), these high-contrast dots are unlikely to be at points of high-electric-field concentration. The original bearded interface, however, while predicted to have a better distribution than the W1 waveguide, performs the worst out of all of the waveguides in the experiment. This is likely related to the interface holes in the design being a source of fabrication error due to their very small size, and also to the surface proximity issues that they introduce beyond those included in our model. The optimized bearded VH waveguide shows a significant improvement in the experimental results in comparison to its unoptimized counterpart, but not the improvement in the proportion of QDs with 90%+ directionality implied by the simulation data. This is likely due a combination of two factors. The first is the high group

indexes of the ideal design not being replicated in experiment, resulting in a lower probability of high-contrast QDs being measured. The second is the interface holes again leading to a reduction in the contrast for reasons described above.

A feature that is present within the statistics for all of the waveguides and that has been seen in other experiments and QD wafers [3] is the asymmetry in the directionality of the QDs measured from the left and right out-couplers of the waveguide. Figures 3(f)–3(i) show examples of QD spectra that fit closely with the predictions of the FDTD simulations shown in Fig. 1(a). These spectra show the expected behavior of the spectra of the right out-coupler (red) and the left out-coupler (blue) are symmetric, mirrored versions of each other, displaying the same directional contrast with opposite intensities. However, Fig. 3(f) shows an example of asymmetric behavior where the contrast as viewed from the left out-coupler is greater than is seen in the right out-coupler. (A discussion of the extent and nature of this asymmetry can be found in the SM, Sec. S6.)

*Conclusion.* We conducted a comparative analysis of conventional and topological waveguides for directional coupling of embedded quantum emitters. Through a combination of experimental characterization of directional coupling and a simulation-based analysis of electric field properties and  $\beta$  factors, we have gained a comprehensive view of the waveguides' individual suitability for directional quantum optics applications. Among the waveguides examined, the glide plane demonstrated the highest proportion of high-directional-contrast QDs, making it well suited for achieving such QDs within a linear waveguide system with randomly positioned QDs. In contrast, while the zigzag interface VH waveguide exhibited good experimental performance by producing a large portion of high-directional-contrast QDs, our modeling showed that regions with high directional contrast within the zigzag waveguide are unlikely to have high  $\beta$  factors.

When considering more complex structures, like ring resonators that require robust transmission around tight bends, topological waveguides emerge as a promising platform for directional quantum optics. Despite the discussed  $\beta$ -factor limitations of the zigzag interface, it is still possible to achieve a high  $\beta$  factor within topological waveguides by using slow light. By combining the high  $\beta$  factors resulting from the slow-light region of the inverse-designed, bearded VH waveguide with appropriate QD registration [3,27,29,30] or site-controlled growth [31,32] techniques, it may be possible to achieve deterministic positioning of QDs at points within the waveguide that exhibit both high directionality and high  $\beta$  factors. This approach presents a pathway towards achieving high-beta-factor, high-directional-contrast QD emission within more complex photonic crystal device geometries.

Exciting future prospects of this research include the realization of separation-independent QD-QD interactions [1,33], super- and subradiant many-body states [34–36], and the formation of large-scale directional spin networks [37] using a conventional or topologically protected photonic platform. Spin [38] and vorticity [39] selective light-matter coupling in the quantum Hall regime is also an intriguing new platform in

which the topological interplay between light and matter can be explored.

Data supporting this study are openly available from the authors upon reasonable request.

*Acknowledgments.* This work was supported by EPSRC Grants No. EP/N031776/1, No. EP/V026496/1, the Quantum Communications Hub EP/T001011/1, and the Natural Sciences and Engineering Council Canada (NSERC). The authors would like to acknowledge helpful discussions with Edo

Waks, Kartik Srinivasan, Nir Rotenberg, Peter Millington-Hotze, and Hamedreza Siampour.

N.J.M., M.J.M., and E.N. designed the photonic structures, which R.D. fabricated. E.C. and P.K.P. grew the sample. N.J.M., M.J.M., X.C., L.H., A.F., and D.H. carried out the measurements and simulations. L.R.W., A.M.F., S.H., M.H., and M.S.S. provided supervision and expertise. N.J.M., M.J.M., X.C. L.H., and E.N. wrote the manuscript, with input from all authors.

- 
- [1] P. Lodahl *et al.*, Chiral quantum optics, *Nature (London)* **541**, 473 (2017).
- [2] I. Söllner *et al.*, Deterministic photon-emitter coupling in chiral photonic circuits, *Nat. Nanotechnol.* **10**, 775 (2015).
- [3] R. J. Coles *et al.*, Chirality of nanophotonic waveguide with embedded quantum emitter for unidirectional spin transfer, *Nat. Commun.* **7**, 11183 (2016).
- [4] A. B. Young *et al.*, Polarization engineering in photonic crystal waveguides for spin-photon entanglers, *Phys. Rev. Lett.* **115**, 153901 (2015).
- [5] S. Mahmoodian, K. Prindal-Nielsen, I. Söllner, S. Stobbe, and P. Lodahl, Engineering chiral light matter interaction in photonic crystal waveguides with slow light, *Opt. Mater. Express* **7**, 43 (2017).
- [6] H. Siampour *et al.*, Observation of large spontaneous emission rate enhancement of quantum dots in a broken-symmetry slow-light waveguide, *npj Quantum Inf.* **9**, 15 (2023).
- [7] S. Barik *et al.*, A topological quantum optics interface, *Science* **359**, 666 (2018).
- [8] J. Ma, X. Xi, and X. Sun, Topological photonic integrated circuits based on valley kink states, *Laser Photonics Rev.* **13**, 1900087 (2019).
- [9] T. Yamaguchi *et al.*, GaAs valley photonic crystal waveguide with light-emitting InAs quantum dots, *Appl. Phys. Express* **12**, 062005 (2019).
- [10] X.-T. He *et al.*, A silicon-on-insulator slab for topological valley transport, *Nat. Commun.* **10**, 872 (2019).
- [11] M. I. Shalaev, W. Walasik, A. Tsukernik, Y. Xu, and N. M. Litchinitser, Robust topologically protected transport in photonic crystals at telecommunication wavelengths, *Nat. Nanotechnol.* **14**, 31 (2019).
- [12] N. Parappurath, F. Alpeggiani, L. Kuipers, and E. Verhagen, Direct observation of topological edge states in silicon photonic crystals: Spin, dispersion, and chiral routing, *Sci. Adv.* **6**, eaaw4137 (2020).
- [13] H. Yoshimi *et al.*, Experimental demonstration of topological slow light waveguides in valley photonic crystals, *Opt. Express* **29**, 13441 (2021).
- [14] M. Jalali Mehrabad, Integrated topological quantum optics, <https://theses.whiterose.ac.uk/29610/> (2021).
- [15] M. J. Mehrabad, S. Mittal, and M. Hafezi, Topological photonics: fundamental concepts, recent developments, and future directions, *Phys. Rev. A* **108**, 040101 (2023).
- [16] S. Barik, A. Karasahin, S. Mittal, E. Waks, and M. Hafezi, Chiral quantum optics using a topological resonator, *Phys. Rev. B* **101**, 205303 (2020).
- [17] M. J. Mehrabad *et al.*, A semiconductor topological photonic ring resonator, *Appl. Phys. Lett.* **116**, 061102 (2020).
- [18] M. J. Mehrabad *et al.*, Chiral topological photonics with an embedded quantum emitter, *Optica* **7**, 1690 (2020).
- [19] L. Gu *et al.*, A topological photonic ring-resonator for on-chip channel filters, *J. Lightwave Technol.* **39**, 5069 (2021).
- [20] M. J. Mehrabad *et al.*, Chiral topological add-drop filter for integrated quantum photonic circuits, *Optica* **10**, 415 (2023).
- [21] C. A. Rosiek *et al.*, Observation of strong backscattering in valley-Hall photonic topological interface modes, *Nat. Photon.* **17**, 386 (2023).
- [22] N. V. Hauff, H. Le Jeannic, P. Lodahl, S. Hughes, and N. Rotenberg, Chiral quantum optics in broken-symmetry and topological photonic crystal waveguides, *Phys. Rev. Res.* **4**, 023082 (2022).
- [23] See Supplemental Material at <http://link.aps.org/supplemental/10.1103/PhysRevResearch.6.L022065> for more information on the waveguide designs, asymmetric directional contrast and the calculation of the  $\beta$ -factor.
- [24] E. Sauer, J. P. Vasco, and S. Hughes, Theory of intrinsic propagation losses in topological edge states of planar photonic crystals, *Phys. Rev. Res.* **2**, 043109 (2020).
- [25] M. Minkov *et al.*, Inverse design of photonic crystals through automatic differentiation, *ACS Photonics* **7**, 1729 (2020).
- [26] S. Manna *et al.*, Surface passivation and oxide encapsulation to improve optical properties of a single GaAs quantum dot close to the surface, *Appl. Surf. Sci.* **532**, 147360 (2020).
- [27] T. Pregolato *et al.*, Deterministic positioning of nanophotonic waveguides around single self-assembled quantum dots, *APL Photonics* **5**, 086101 (2020).
- [28] B. Lang, D. M. Beggs, and R. Oulton, Time-reversal constraint limits unidirectional photon emission in slow-light photonic crystals, *Philos. Trans. R. Soc. A* **374**, 20150263 (2016).
- [29] L. Sapienza, M. Davanço, A. Badolato, and K. Srinivasan, Nanoscale optical positioning of single quantum dots for bright and pure single-photon emission, *Nat. Commun.* **6**, 7833 (2015).
- [30] P. Schnauber *et al.*, Deterministic integration of quantum dots into on-chip multimode interference beamsplitters using in situ electron beam lithography, *Nano Lett.* **18**, 2336 (2018).
- [31] J. Große, M. von Helversen, A. Koulas-Simos, M. Hermann, and S. Reitzenstein, Development of site-controlled quantum dot arrays acting as scalable sources of indistinguishable photons, *APL Photonics* **5**, 096107 (2020).

- [32] K. D. Jöns *et al.*, Triggered indistinguishable single photons with narrow line widths from site-controlled quantum dots, *Nano Lett.* **13**, 126 (2013).
- [33] C. Gonzalez-Ballester, A. Gonzalez-Tudela, F. J. Garcia-Vidal, and E. Moreno, Chiral route to spontaneous entanglement generation, *Phys. Rev. B* **92**, 155304 (2015).
- [34] A. Tiranov *et al.*, Collective super- and subradiant dynamics between distant optical quantum emitters, *Science* **379**, 389 (2023).
- [35] J.-H. Kim, S. Aghaieimebodi, C. J. K. Richardson, R. P. Leavitt, and E. Waks, Super-radiant emission from quantum dots in a nanophotonic waveguide, *Nano Lett.* **18**, 4734 (2018).
- [36] J. Q. Grim *et al.*, Scalable in operando strain tuning in nanophotonic waveguides enabling three-quantum-dot superradiance, *Nat. Mater.* **18**, 963 (2019).
- [37] H. Pichler, T. Ramos, A. J. Daley, and P. Zoller, Quantum optics of chiral spin networks, *Phys. Rev. A* **91**, 042116 (2015).
- [38] D. G. Suarez-Forero *et al.*, Spin-selective strong light-matter coupling in a 2D hole gas-microcavity system, *Nat. Photon.* **17**, 912 (2023).
- [39] D. Session *et al.*, Optical pumping of electronic quantum Hall states with vortex light, [arXiv:2306.03417](https://arxiv.org/abs/2306.03417).